Target *K*-vacancy production by 2.5 to 25 MeV/amu Ar, Kr, and Xe ions

R. L. Watson, Y. Peng, V. Horvat, and A. N. Perumal*
Cyclotron Institute and Department of Chemistry, Texas A&M University, College Station, Texas 77843-3366, USA
(Received 1 September 2006; published 15 December 2006)

Cross sections have been measured for $K\alpha$ x-ray production in targets of Al, Ti, Cu, Zr, Ag, Sm, and Ta by Ar, Kr, and Xe ions ranging in energy from 2.5 to 25 MeV/amu. In addition, the degree of simultaneous *L*-shell ionization and the enhancement of the $K\alpha$ diagram lines due to secondary ionization processes were assessed by performing high-resolution spectral measurements on Al, Ti, V, Co, and Cu targets. This information was used to correct for the $K\alpha$ x-ray yield produced by electron bombardment and photoionization, and to calculate the fluorescence yields needed to convert the $K\alpha$ x-ray production cross sections into *K*-vacancy production cross sections. The resulting cross sections were compared with the predictions of the perturbed stationary state approximation with corrections for projectile energy loss, Coulomb deflection, and relativistic effects (ECPSSR theory). Also, the scaling properties of the $K\alpha$ x-ray production cross sections were examined and a semiempirical (universal) curve was deduced that reproduces the measured cross sections to within ±30% on average.

DOI: 10.1103/PhysRevA.74.062709 PACS number(s): 34.50.Fa

I. INTRODUCTION

Inner-shell vacancy production in heavy ion-atom collisions is difficult to treat theoretically because of the many-body nature of the process. Generally, the projectile is not fully stripped of its electrons, and hence both electron-nucleus and electron-electron interactions must be taken into account. Moreover, several distinct mechanisms may contribute to vacancy production in the target, including direct Coulomb ionization and excitation, electron capture by the projectile, and, in nearly symmetric collisions at low relative velocities, electron promotion via quasimolecular level crossings. The process is further complicated by the simultaneous ejection of electrons from higher shells leaving the target in a multiply ionized final state. As a result of this complexity, accurate theoretical methods for calculating inner-shell vacancy production cross sections for collisions involving projectiles with atomic numbers (Z_1) of the order of 18 or more have not yet been developed.

Although, in the past four decades, a great deal of attention has been directed toward the investigation of *K*-vacancy production cross sections for collisions involving projectiles with $Z_1=10$ or less, relatively little work has been performed with higher-Z_1 projectiles. Early experiments with Br, Kr, I, Xe, and Pb ions were described by Meyerhof and co-workers in a pioneering series of papers [1–4]. These authors examined the target atomic number (Z_2) dependence of *K*-vacancy production cross sections for fixed Z_1 and E_1 (where E_1 is the projectile energy) and noted features relating to the transition from an atomic domain for asymmetric collision partners to a molecular domain for symmetric collision systems. Somewhat later, Anholt *et al.* [5] investigated the target dependence of inner-shell ionization in collisions with Ne, Kr, Xe, La, and U ions at relativistic energies. General agreement (at the level of ~30%) was found between their measured cross sections and those predicted by the plane-wave Born approximation (PWBA).

More recently, Z_1-dependence studies of *K*-vacancy production in Cu [6] and Al [7] targets at 10 MeV/amu have shown large discrepancies between experimental results and the predictions of the ECPSSR theory (perturbed stationary-state approximation with corrections for projectile energy loss, Coulomb deflection, and relativistic effects [8,9]), modified to include electron capture [10]. This work has revealed that beyond $Z_1=10$, in the case of Al, and $Z_1=18$, in the case of Cu, the theoretical cross sections rise much faster than the experimental cross sections. At $Z_1=83$, the theoretical cross sections were 15 and 18 times higher than the experimental cross sections for Al and Cu targets, respectively. These results highlight the need for a larger database to enable the establishment of semiempirical scaling laws capable of systematizing *K*-vacancy production cross sections for a wide variety of collision systems.

The present experiments were undertaken to examine the dependence of *K*-vacancy production by heavy ions on the projectile/target speed ratio ($V=v_1/v_{2K}$, where v_1 is the projectile speed and v_{2K} is the target *K*-electron average speed). The ultimate goal was to develop a semiempirical method for estimating cross sections for similar collision systems. Measurements were performed for 2.5 to 25 MeV/amu ($v_1=10.0$ to 31.1 a.u.) Ar, Kr, and Xe ions colliding with targets of Al, Ti, Cu, Zr, Ag, Sm, and Ta ($v_{2K}=10.7$ to 63.0 a.u.). Absolute *K* x-ray yields were obtained using an Si(Li) detector and high-resolution spectra of Al, Ti, V, Co, and Cu *K* x rays were recorded with a 12.7 cm Johansson-type curved crystal spectrometer to provide information relating to corrections for multiple ionization and x-ray production by secondary processes.

II. EXPERIMENTAL METHODS

Beams of 2.5, 4.0, 6.0, 9.9, 15.0, 20.0, and 24.8 MeV/amu Ar, Kr, and Xe ions were extracted from the Texas A&M K500 superconducting cyclotron and focused at the

*Present address: Synchrotron Radiation Center, 3731 Schneider Drive, Stoughton, WI 53589.

TABLE I. Target and reference foil thicknesses in units of mg/cm^2 (corrected for the 45° inclination angle).

Target	Thickness	Reference foil	Thickness
Al	0.848		
Ti	1.234		
Cu	1.639		
Zr	1.571		
Ag	1.493	Cu	3.549
Sm	1.343	Ag	3.917
Sm	5.896	Ag	3.973
Ta	1.226	Ag	3.139
Ta	2.602	Ag	3.973

target position. The incident charge states over the stated energy range varied from 4+ to 11+ for Ar, 8+ to 23+ for Kr, and 13+ to 31+ for Xe. For the K x-ray yield measurements, two 1-mm-diam collimators were then inserted to precisely define the beam spot on the target. The targets, consisting of self-supported metallic foils having thicknesses determined from their measured weights and areas (see Table I), were obtained from Goodfellow Corp. [11]. The targets were thick enough to insure full charge-state equilibration of the projectile ions, but thin enough that energy loss was not a major concern (except in the case of the thicker Sm target at the lower energies). They were mounted in a target wheel oriented at a 45° angle relative to both the incident ion beam and an Si(Li) x-ray detector that viewed the front of the target. Absolute K x-ray yields were obtained by counting the corresponding numbers of incident ions using a plastic scintillator detector mounted directly behind the target. A coincidence requirement was imposed on the x-ray and particle signals in order to eliminate any uncertainties concerning the efficiency of the particle detector.

Absolute K x-ray yields could not be measured for the Sm and Ta targets by direct particle counting because their K x-ray production cross sections were too low to provide sufficient x-ray counting statistics at usable particle rates. This same problem was also encountered for the Ag targets at 2.5 and 4.0 MeV/amu. In the case of Ag, a reference foil of Cu (see Table I) was mounted behind the target in the same holder and the absolute yield of Cu K x rays was determined by direct particle counting, as described above. Then the particle detector was removed so that the particle rate could be increased and a thin (12.6 mg/cm^2) Al absorber was placed in front of the Si(Li) detector to absorb low energy (L) x rays. Finally, an x-ray spectrum containing both the target and the reference K x rays was recorded at an increased particle rate sufficient to provide adequate target K x-ray counting statistics. In the case of Sm and Ta, reference foils of Ag (see Table I) and a three-step procedure were employed. In the first step, the absolute yield of target $L\alpha$ x rays was determined by direct particle counting. In the next step, the particle detector was removed, the thin Al absorber placed in front of the Si(Li) detector to absorb target M x

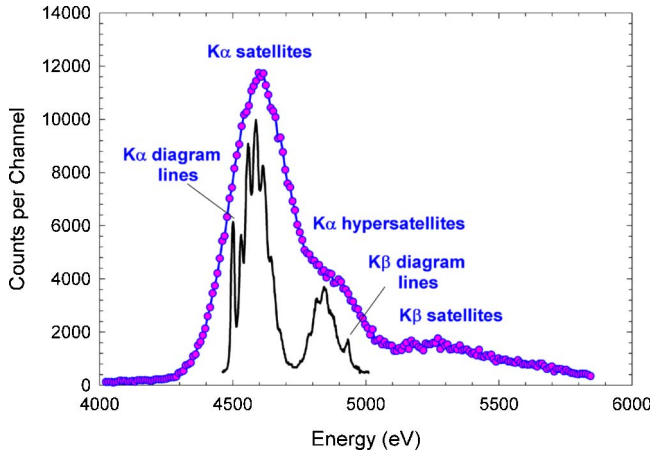

FIG. 1. (Color online) Comparison of Ti $K\alpha$ x-ray spectra, excited by 25 MeV/amu Kr ions, obtained with the low-resolution Si(Li) detector and the high-resolution curved crystal spectrometer. The various components that contribute to the spectra are indicated.

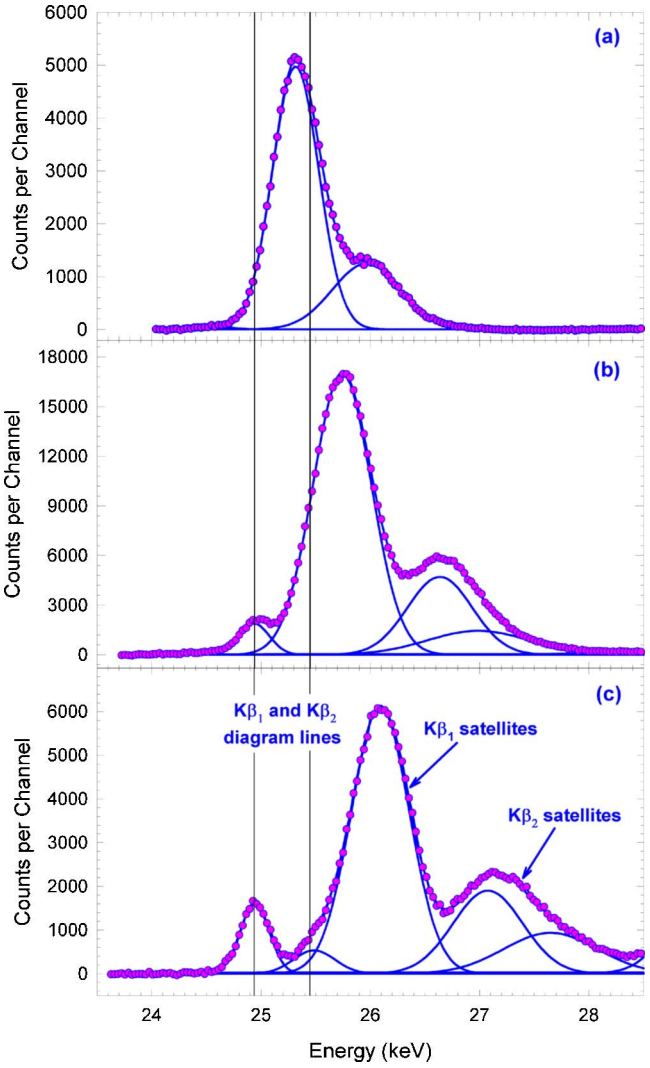

FIG. 2. (Color online) Spectra, obtained with the Si(Li) detector, of the $K\beta$ region of Ag excited by 25 MeV/amu (a) Ar, (b) Kr, and (c) Xe ions. The two vertical lines delineate the average energy positions of the $K\beta_1$ and $K\beta_2$ diagram lines.

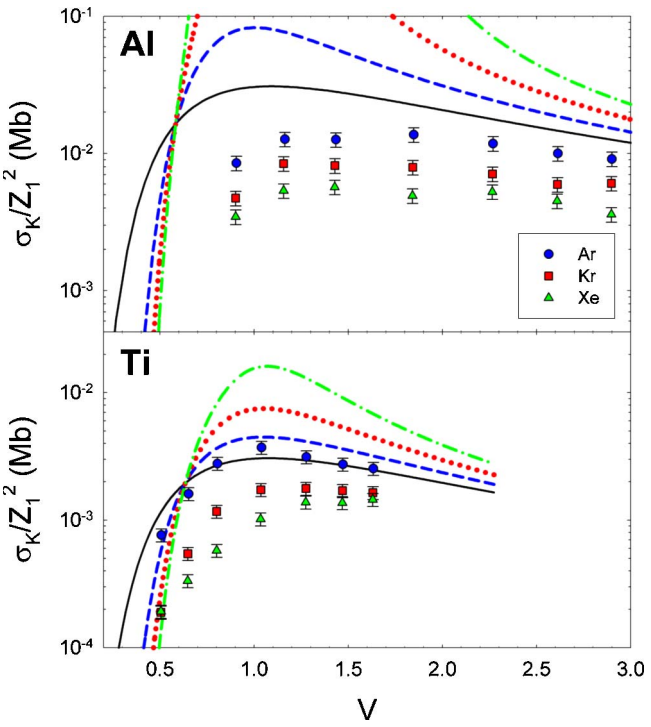

FIG. 3. (Color online) Comparison of the experimental results for Al and Ti with the predictions of the ECPSSR theory. The theoretical curves are for Ar (blue dashed), Kr (red dotted), and Xe (green dot-dashed) projectiles. The solid curve shows the ECPSSR predictions for protons.

rays, and the spectrum of target L x rays plus reference K x rays was recorded at a particle rate sufficient to provide adequate Ag K x-ray counting statistics. Finally, in the last step, the thin Al absorber was replaced with a thick (355 mg/cm^2) Al absorber to reduce the target L x-ray intensity, and the spectrum of target K x rays plus reference foil K x rays was recorded at a particle rate sufficient to provide adequate target K x-ray counting statistics.

The curved crystal spectrometer measurements were performed in another vacuum chamber located approximately one meter downstream from the Si(Li) detector and for these measurements, a 3-mm-diam collimator was employed to define the beam spot on the target. The Al spectra were recorded in first order using an EDDT (ethylenediamine ditartrate) crystal, while the Ti and V (first order) spectra and the Co and Cu (second order) spectra were recorded using an LiF(200) crystal. Additional details of the high-resolution measurements are given in Ref. [6].

A comparison of Ti K x-ray spectra obtained with the Si(Li) detector and the crystal spectrometer, excited by 25 MeV/amu Kr ions, is shown in Fig. 1. These spectra clearly show the five components of a typical K x-ray spectrum excited by heavy-ion bombardment; namely, a prominent peak containing (mostly) the $K\alpha$ diagram lines, a series of satellite peaks containing $K\alpha$ x rays emitted by target atoms having one to seven spectator L vacancies in addition to a K vacancy, a series of hypersatellite peaks containing $K\alpha$ x rays emitted by target atoms having one to seven spectator L vacancies plus two K vacancies, a peak containing the

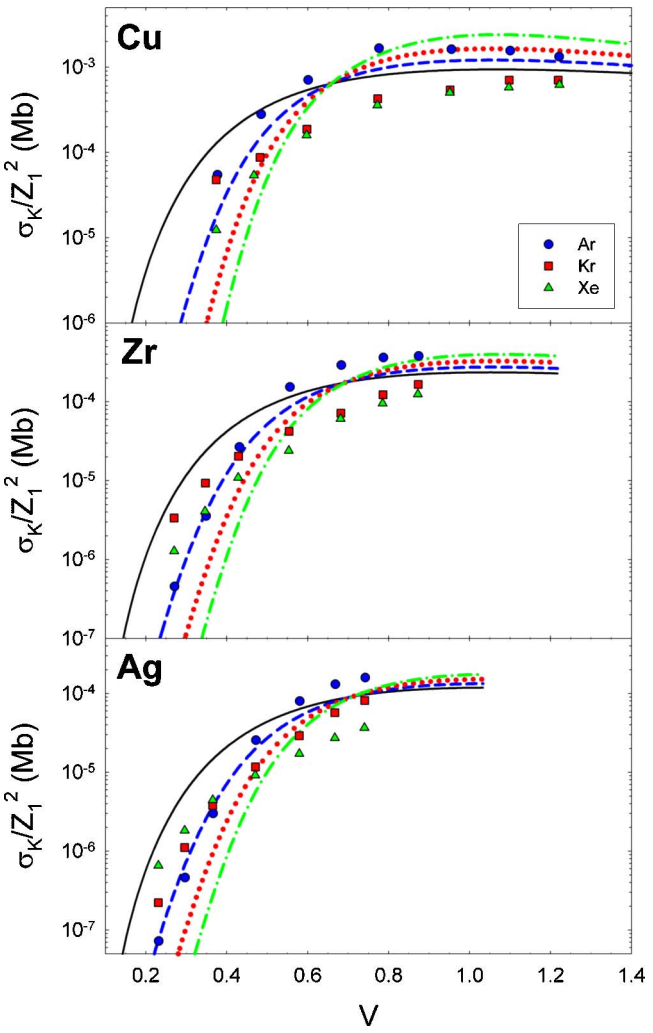

FIG. 4. (Color online) Comparison of the experimental results for Cu, Zr, and Ag with the predictions of the ECPSSR theory. The theoretical curves are for Ar (blue dashed), Kr (red dotted), and Xe (green dot-dashed) projectiles. The solid curve shows the ECPSSR predictions for protons. (The experimental error bars are smaller than the size of the data points.)

$K\beta$ diagram lines, and [in the Si(Li) spectrum] a broad peak containing the $K\beta$ satellite x rays. The diagram line peaks contain K x rays emitted by atoms with zero spectator L vacancies and, in the Fig. 1 spectra, they are produced primarily by energetic electrons and photons generated in ion-atom collisions [6,12]. Since the diagram x rays cannot be resolved in the Si(Li) detector spectra, the high-resolution spectra are used to determine the corrections that must be applied to the x-ray yields [measured with the Si(Li) detector] to account for contributions from secondary ionization processes.

The product of the Si(Li) detector efficiency (ε) and solid-angle fraction (Ω) was measured at 12 energies ranging from 11.9 to 81.0 keV using calibrated radioactive sources of ^{57}Co, ^{241}Am, and ^{133}Ba. The low-energy region (below 11.9 keV) was calibrated by comparing the measured yields of K x rays produced in thin targets of Al, Si (SiO_2), Cl (KCl), K (KCl), Ti, and Cu by bombardment of 10 MeV

TABLE II. Cross sections for K-vacancy production by Ar ions. (Numbers in parentheses indicate powers of ten.)

Target ω_0	E/M MeV/amu	R_s (%)	$\omega_{K\alpha}/\omega_0$	σ_{tot} (Mb)	Target ω_0	E/M MeV/amu	R_s (%)	$\omega_{K\alpha}/\omega_0$	σ_{tot} (Mb)
Al	2.33	7.81	1.79	2.75(0)	Ti	2.30	1.90	1.49	2.47(−1)
0.0382	3.85	9.10	1.72	4.10(0)	0.199	3.81	2.47	1.45	5.22(−1)
	5.87	9.83	1.65	4.08(0)		5.84	2.93	1.39	9.00(−1)
	9.80	9.39	1.53	4.43(0)		9.78	3.42	1.32	1.20(0)
	14.92	8.00	1.41	3.83(0)		14.90	3.76	1.25	1.01(0)
	19.94	7.49	1.33	3.24(0)		19.92	3.98	1.21	8.87(−1)
	24.75	6.98	1.27	2.95(0)		24.73	4.14	1.18	8.22(−1)
Cu	2.27	1.50	1.16	1.77(−2)	Zr	2.30	0	1.04	1.47(−4)
0.399	3.78	2.12	1.15	9.07(−2)	0.616	3.81	0	1.04	1.16(−3)
	5.81	2.66	1.14	2.30(−1)		5.83	0	1.04	8.67(−3)
	9.75	3.32	1.12	5.41(−1)		9.77	0	1.04	5.00(−2)
	14.88	3.83	1.10	5.26(−1)		14.89	0	1.03	9.46(−2)
	19.90	4.19	1.08	5.07(−1)		19.91	0	1.03	1.18(−1)
	24.71	4.46	1.07	4.32(−1)		24.72	0	1.03	1.23(−1)
Ag	2.33	1.48	1.01	2.34(−5)	Sm	3.50	0	1.00	9.74(−6)
0.685	3.84	1.63	1.03	1.49(−4)	0.738	5.52	0	1.00	4.76(−5)
	5.86	1.80	1.03	9.73(−4)		9.49	0	1.00	3.39(−4)
	9.78	2.01	1.03	8.29(−3)		14.79	0	1.00	1.65(−3)
	14.90	2.05	1.03	2.60(−2)		19.71	0	1.00	3.60(−3)
	19.92	1.83	1.03	4.26(−2)		24.65	0	1.00	5.87(−3)
	24.73	1.37	1.03	5.15(−2)					
Ta	2.29	0	1.00	3.17(−6)					
0.751	3.78	0	1.00	6.96(−6)					
	5.80	0	1.00	1.84(−5)					
	9.73	0	1.00	7.03(−5)					
	14.88	0	1.00	3.21(−4)					
	19.88	0	1.00	7.38(−4)					
	24.72	0	1.00	1.36(−3)					

protons with the yields calculated from ionization cross sections predicted by the ECPSSR theory. An $\Omega\varepsilon$ curve was then obtained by fitting all of the calibration points to a standard efficiency function, as described in Ref. [6]. The uncertainty in $\Omega\varepsilon$ is estimated to be ±3% at energies above 8.0 keV and ±10% below this energy. The x-ray transmission probability as a function of x-ray energy was determined for each of the two Al absorbers by measuring photon yields from the ^{241}Am source with and without the absorbers present.

III. ANALYSIS AND RESULTS

The *total* K-vacancy production cross section σ_K may be expressed as

$$\sigma_K = \sigma_K^1 + 2\sigma_K^2, \tag{1}$$

where σ_K^1 is the single K-vacancy production cross section and σ_K^2 is the double K-vacancy production cross section. It may be determined by dividing the cross section for $K\alpha$ x-ray production ($\sigma_{K\alpha}$) by $\omega_{K\alpha}$, the average $K\alpha$ fluorescence yield. To obtain $\sigma_{K\alpha}$, the total yield of primary $K\alpha$ x rays $N_{K\alpha}$ must be extracted from the measured spectra. Assuming the average fluorescence yield is the same for the decay of both single and double K-vacancy states, the creation of a double K-vacancy state will result in the emission of a $K\alpha$ hypersatellite x ray and a $K\alpha$ satellite x ray with equal probabilities. Therefore, the factor of 2 in Eq. (1) is automatically taken into account. The yield of primary $K\alpha$ x rays is

$$N_{K\alpha} = N_{\text{tot}} - N_s, \tag{2}$$

where

$$N_{\text{tot}} = N_d + N_{\text{sat}} + N_{\text{hsat}}. \tag{3}$$

In the above equations, N_s is the yield of $K\alpha$ x rays produced by secondary processes (i.e., electron bombardment and photoionization), N_d is the yield of the $K\alpha$ diagram x rays, N_{sat} is the yield of $K\alpha$ satellite x rays, and N_{hsat} is the yield of $K\alpha$ hypersatellite x rays.

Peak-fitting analysis of the Si(Li) detector spectra provided the quantities N_1 and N_{hsat}, where $N_1 = N_d + N_{\text{sat}}$. In the cases of Al, Ti, and Cu, analysis of the high-resolution spec-

TABLE III. Cross sections for *K*-vacancy production by Kr ions. (Numbers in parentheses indicate powers of ten.)

Target ω_0	E/M MeV/amu	R_s (%)	$\omega_{K\alpha}/\omega_0$	σ_{tot} (Mb)	Target ω_0	E/M MeV/amu	R_s (%)	$\omega_{K\alpha}/\omega_0$	σ_{tot} (Mb)
Al	2.31	15.0	1.72	6.11(0)	Ti	2.28	3.05	1.66	2.45(−1)
0.0382	3.81	15.1	1.73	1.09(1)	0.199	3.77	4.01	1.64	7.06(−1)
	5.83	15.1	1.73	1.06(1)		5.78	4.82	1.62	1.51(0)
	9.76	15.1	1.73	1.03(1)		9.72	5.68	1.57	2.24(0)
	14.88	14.4	1.70	9.18(0)		14.84	6.26	1.53	2.29(0)
	19.90	13.3	1.65	7.70(0)		19.86	6.62	1.49	2.20(0)
	24.71	11.7	1.59	7.84(0)		24.68	6.89	1.45	2.13(0)
Cu	2.24	2.98	1.24	6.18(−2)	Zr	2.28	0.00	1.07	4.35(−3)
0.399	3.73	4.34	1.24	1.13(−1)	0.616	3.77	0.76	1.07	1.21(−2)
	5.75	5.71	1.23	2.42(−1)		5.78	2.29	1.07	2.64(−2)
	9.68	7.46	1.21	5.52(−1)		9.70	4.65	1.07	5.46(−2)
	14.81	8.81	1.20	6.98(−1)		14.83	6.45	1.07	9.32(−2)
	19.83	9.61	1.18	9.12(−1)		19.85	6.81	1.06	1.59(−1)
	24.65	10.13	1.17	9.14(−1)		24.67	5.85	1.06	2.15(−1)
Ag	2.31	0.00	1.05	2.88(−4)	Sm	3.42	0	1.00	8.27(−6)
0.685	3.80	1.18	1.06	1.44(−3)	0.738	5.85	0	1.00	1.01(−4)
	5.81	2.84	1.06	4.90(−3)		9.31	0	1.00	4.80(−4)
	9.73	5.37	1.06	1.52(−2)		14.68	0	1.00	2.32(−3)
	14.85	7.25	1.06	3.77(−2)		19.52	0	1.00	6.71(−3)
	19.87	7.52	1.06	7.37(−2)		24.54	0	1.00	1.35(−2)
	24.68	6.33	1.06	1.05(−1)					
Ta	3.74	0	1.00	9.69(−6)					
0.751	5.87	0	1.00	2.34(−5)					
	9.65	0	1.00	1.01(−4)					
	14.81	0	1.00	4.53(−4)					
	19.80	0	1.00	1.36(−3)					
	24.63	0	1.00	2.93(−3)					

tra (see Refs. [6,13]) supplied the ratio $R_s = N_s/N_{tot}$ and this, in combination with Eq. (2) gives

$$N_{K\alpha} = N_{tot}(1 - R_s). \tag{4}$$

In the cases of Zr and Ag, for which high-resolution spectra were not obtainable with the curved crystal spectrometer, R_s was determined using the $K\beta_1$ diagram x rays. Spectra of the $K\beta$ x-ray region of Ag, recorded with the Si(Li) detector, are shown in Fig. 2. In the spectrum excited by Ar ions, there is no indication of any significant contribution from the $K\beta$ diagram lines. This is not surprising since Ar K x rays cannot photoionize the Ag K shell and the yield of secondary electrons capable of ionizing the Ag K shell is expected to be low. However, the spectra excited by Kr and Xe ions both contain enhanced $K\beta_1$ diagram peaks excited by secondary ionization processes. Their intensities, together with theoretical values of the $K\beta_1$ to $K\alpha$ intensity ratio [14], enabled the determination of R_s. Corrections for secondary ionization processes were found to be negligible for the Sm and Ta targets.

The usual corrections for self-absorption in the targets were applied to the measured x-ray yields using mass absorption coefficients from the tabulation of Hubbell and Seltzer [15]. These corrections had to be performed channel by channel for the Al and Ti targets to account for the affects of the K absorption edges, which cut into the $K\alpha$ satellite and $K\alpha$ hypersatellite distributions, respectively. In addition, it was necessary to convolve the absorption curves with the detector resolution function to properly represent the absorption edges.

Because the $K\alpha$ fluorescence yield depends on the degree of ionization, it was necessary to calculate the average fluorescence yields used to convert the $K\alpha$ x-ray production cross sections into K-vacancy production cross sections. This was accomplished by using the procedure described in Ref. [16] to compute the average $K\alpha$ fluorescence yield as a function of the apparent average L-vacancy fraction p_L^x, defined by

$$p_L^x = \frac{1}{8}\sum_{n=1}^{8} n(I_n/I_{tot}), \tag{5}$$

where I_n is the $K\alpha$ satellite intensity corresponding to n L vacancies and

TABLE IV. Cross sections for K-vacancy production by Xe ions. (Numbers in parentheses indicate powers of ten.)

Target ω_0	E/M MeV/amu	R_s (%)	$\omega_{K\alpha}/\omega_0$	σ_{tot} (Mb)	Target ω_0	E/M MeV/amu	R_s (%)	$\omega_{K\alpha}/\omega_0$	σ_{tot} (Mb)
Al	2.31	14.1	1.71	1.01(1)	Ti	2.28	5.85	1.70	5.61(−1)
0.0382	3.81	18.0	1.72	1.55(1)	0.199	3.76	7.32	1.69	9.75(−1)
	5.82	19.4	1.73	1.66(1)		5.77	8.39	1.68	1.68(0)
	9.74	19.4	1.74	1.44(1)		9.69	9.29	1.65	2.98(0)
	14.86	17.9	1.74	1.52(1)		14.82	9.64	1.63	4.02(0)
	19.87	16.4	1.74	1.31(1)		19.83	9.69	1.60	3.99(0)
	24.69	14.4	1.72	1.16(1)		24.65	9.64	1.58	4.24(0)
Cu	2.24	2.09	1.26	3.60(−2)	Zr	2.28	0.00	1.08	3.75(−3)
0.399	3.50	3.04	1.25	1.56(−1)	0.616	3.76	0.97	1.08	1.19(−2)
	5.73	4.35	1.26	4.64(−1)		5.76	2.95	1.08	3.19(−2)
	9.65	5.99	1.25	1.04(0)		9.68	6.21	1.08	6.99(−2)
	14.77	7.39	1.24	1.47(0)		14.80	9.21	1.08	1.78(−1)
	19.80	8.28	1.23	1.68(0)		19.82	10.77	1.08	2.79(−1)
	24.78	8.89	1.22	1.82(0)		24.63	10.98	1.07	3.64(−1)
Ag	2.31	3.71	1.07	1.92(−3)	Sm	3.41	0	1.00	8.54(−5)
0.685	3.80	4.74	1.07	5.35(−3)	0.738	5.83	0	1.00	8.39(−4)
	5.80	6.02	1.08	1.30(−2)		9.34	0	1.00	2.24(−3)
	9.70	8.20	1.08	2.68(−2)		14.61	0	1.00	6.07(−3)
	14.82	10.42	1.07	5.00(−2)		19.42	0	1.00	9.50(−3)
	19.84	11.88	1.07	7.97(−2)		24.68	0	1.00	1.56(−2)
	24.65	12.62	1.07	1.07(−1)					
Ta	5.86	0	1.00	6.44(−5)					
0.751	9.62	0	1.00	2.41(−4)					
	14.78	0	1.00	9.09(−4)					
	19.76	0	1.00	2.18(−3)					
	24.70	0	1.00	3.90(−3)					

$$I_{\text{tot}} = \sum_{n=0}^{8} I_n. \tag{6}$$

Experimental values of p_L^x were determined directly from the high-resolution spectra for Al, Ti, and Cu. The p_L^x values for the other targets were calculated using a semiempirical universal function given by [13,17]

$$p_L^x = a/[1 + (b/X)^c], \tag{7}$$

where $a=0.535$, $b=2.10$, $c=1.94$, and X is the universal variable of the geometric model developed by Sulik *et al.* [18]. The universal variable is defined as

$$X = 4V[G(V)]^{1/2}Z_1/(nv_1), \tag{8}$$

where $G(V)$ is the scaled velocity function of the binary encounter approximation, as given in Ref [19] and n is the principal quantum number (2 in the present case).

The K-vacancy production cross sections and parameters used to derive them from the measured $K\alpha$ x-ray yields are listed in Tables II–IV. In these tables, the quantity labeled ω_0 is the normal $K\alpha$ fluorescence yield for the decay of a single K-vacancy state having zero spectator vacancies. The listed values of ω_0 were derived from the relation $\omega_0=\omega_K(1+R_{\beta/\alpha})^{-1}$ using the total K fluorescence yields ω_K given in Table 8 of Hubbell *et al.* [20] and the theoretical $K\beta$ to $K\alpha$ intensity ratios $R_{\beta/\alpha}$ of Scofield [14]. The values of $\omega_{K\alpha}/\omega_0$ are those calculated in the present work for the corresponding values of p_L^x. The E/M values listed in these tables have been corrected for energy loss in the targets, taking into account the energy dependence of the vacancy production cross sections and the depth dependence of the x-ray transmission probabilities. It should be noted that the cross sections in Tables II–IV are *total* K-vacancy production cross sections as defined by Eq. (1), whereas the cross sections given in Refs. [6,7] are cross sections for *single* K-vacancy production (σ_K^1). The experimental uncertainties are summarized in Table V .

IV. DISCUSSION

A. Comparison with theory

The K-vacancy production cross sections divided by Z_1^2 are compared with the predictions of the ECPSSR theory in Figs. 3–5. The ECPSSR cross sections include contributions

TABLE V. Average experimental uncertainties of the *K*-vacancy production cross sections.

Target	*E*/*M* (MeV/amu)	Uncertainty (%)
Al	2.0–25	12
Ti	2.0–25	11
Cu	2.0–25	5.3
Zr	2.0–25	6.3
Ag	2.0–4.0	12
Ag	>4.0	4.9
Sm	2.0–4.0	13
Sm	>4.0	11
Ta	2.0–4.0	12
Ta	>4.0	9.3

from both direct *K*-shell ionization [9] and *K*-electron capture to the projectile [10]. In the electron-capture calculations, the projectiles were assumed to have equilibrated ground-state electron configurations. Also shown in the cross-section figures are ECPSSR cross-section curves for proton projectiles.

The experimental results for Ar projectiles lie far below the theoretical predictions for Al, but for Ti, they are only 23% (on average) below, except for the point at the lowest *V*, which is 30% above. The Cu data are all substantially above

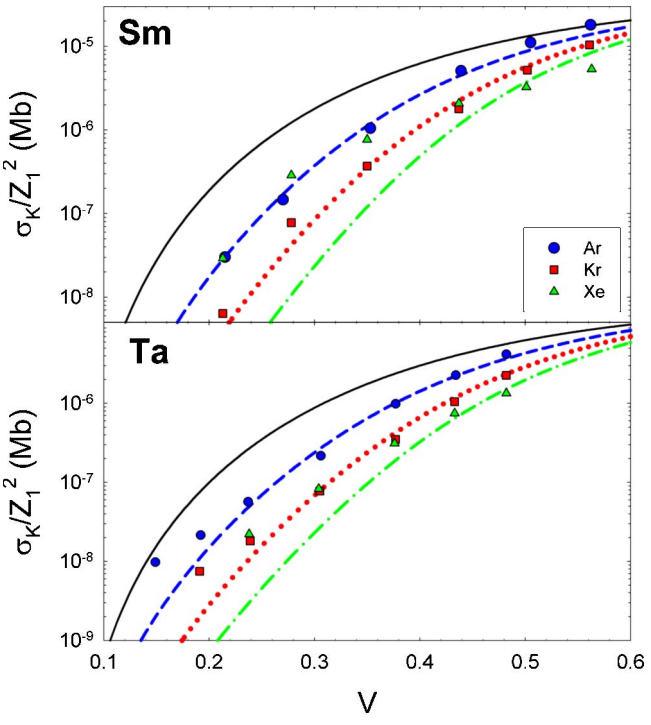

FIG. 5. (Color online) Comparison of the experimental results for Sm and Ta with the predictions of the ECPSSR theory. The theoretical curves are for Ar (blue dashed), Kr (red dotted), and Xe (green dot-dashed) projectiles. The solid curve shows the ECPSSR predictions for protons. (The experimental error bars are smaller than the size of the data points.)

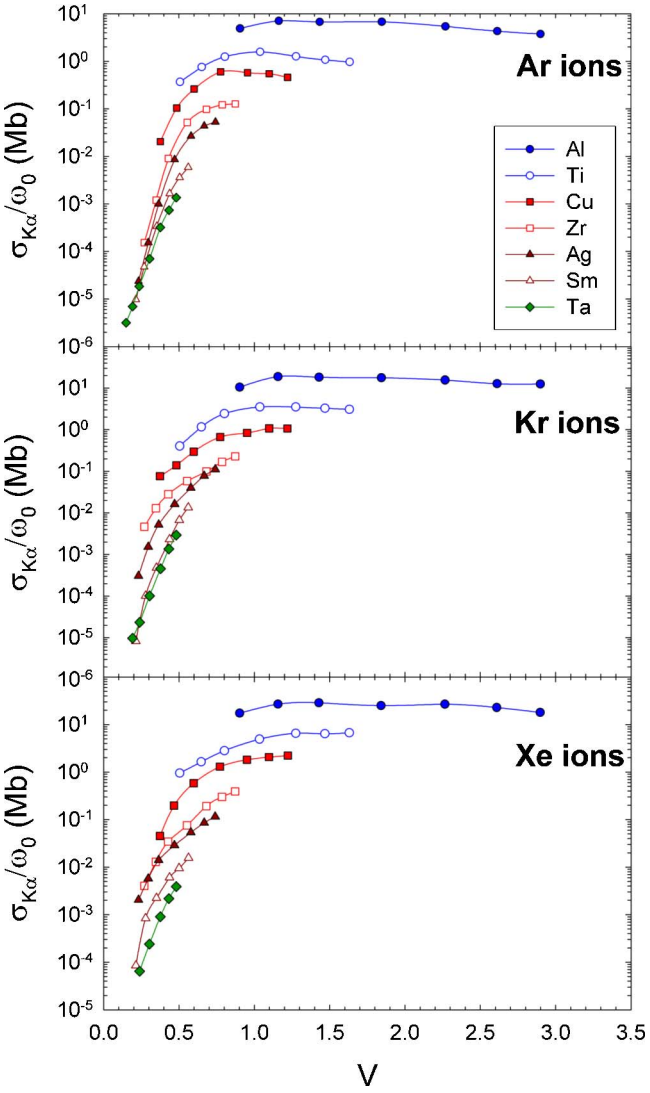

FIG. 6. (Color online) The sets of $K\alpha$ x-ray production cross sections divided by the single-vacancy fluorescence yields, as a function of speed ratio (shown separately for each projectile).

the theoretical curve (65% on average), but the Zr and Ag data agree well with theory at *V* below 0.5 and rise above the theoretical curves beyond.

The experimental results for Kr and Xe projectiles on the targets Al through Ag are in very poor agreement with the theoretical curves. In the cases of the Al and Ti targets, the data points all lie far below the theoretical curves. For the Cu, Zr, and Ag targets, the data points start out considerably above the theoretical curves at low *V*, cross over at some intermediate *V*, and fall below at high values of *V*. The experimental data points for Kr on Sm and those for Kr on Ta (except for those at the lowest two values of *V*) agree quite well with theory. Evidence of cross-section enhancement due to contributions from the molecular-orbital level-crossing mechanism can be seen at *V* below 0.5 in the data for Kr on Cu and Zr, and in the data for Xe on Ag, Sm, and Ta, as has been demonstrated in previous experiments at 10 MeV/amu [21,22].

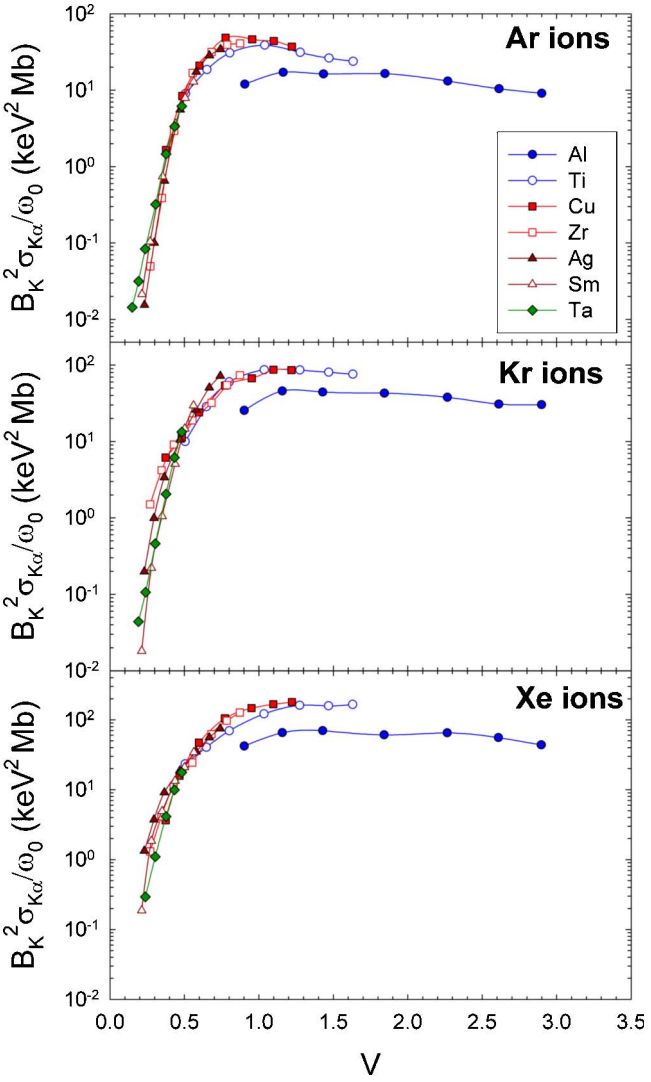

FIG. 7. (Color online) The data in Fig. 6 multiplied by the scaling factor B_K^2 for each target, as a function of speed ratio (shown separately for each projectile).

B. Scaling of the cross sections

In view of the fact that reliable theoretical methods for predicting cross sections for K x-ray production in heavy ion-atom collisions have yet to be developed, and because these cross sections are of practical use in analytical applications and for beam monitoring in experiments with heavy ions, it is desirable to examine scaling relations that might provide a means for their estimation. First-order descriptions of inner-shell ionization based on the PWBA as well as the classical binary encounter approximation (BEA) predict that target K-shell ionization cross sections are proportional to the square of the projectile effective charge (Z_{eff}^2) divided by the square of the target-electron binding energy (B_K^2) times a function that defines the V dependence of the collision process. Therefore, a plot of the K-shell ionization cross section multiplied by B_K^2/Z_{eff}^2 versus V should define a universal function that depends only on V. This type of scaling has been found to work reasonably well for proton and alpha particle projectiles with Z_{eff} taken to equal Z_1 [23].

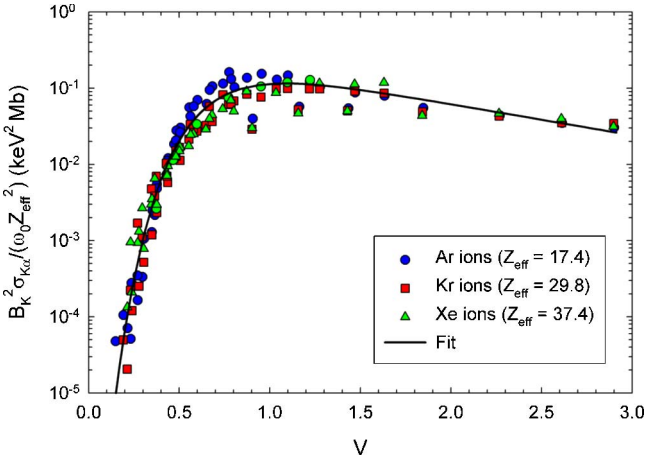

FIG. 8. (Color online) The fully scaled $K\alpha$ x-ray production cross sections as a function of speed ratio. A semiempirical "universal" curve has been fit to the data points.

In the present case involving heavy-ion projectiles, the goal of providing a convenient scaling method for estimating K x-ray production cross sections is obscured by the fluorescence yield factor (which depends on the degree of multiple ionization) since its calculation is difficult and relies on a number of untested approximations and assumptions. Therefore, in the present treatment, it was decided to replace the calculated fluorescence yield $\omega_{K\alpha}$ with the single-vacancy fluorescence yield ω_0 and, in effect, consider it to be part of the overall scaling factor. The effectiveness of the B_K^2/ω_0 scaling factor in accounting for the target dependence of the cross sections is demonstrated in Figs. 6 and 7. In Fig. 6, where the $K\alpha$ x-ray production cross section divided by ω_0 is plotted as a function of V, it is apparent that the data points for the various targets define individual curves and that these curves differ for each projectile. When the data in Fig. 6 are multiplied by B_K^2, as shown in Fig. 7, the individual curves blend together (with the exception of the Al data) to approximately define a common target curve for each projectile.

In seeking to account for the projectile dependence of the $K\alpha$ x-ray production cross sections, it is obvious from Figs. 3–5 that setting $Z_{\mathrm{eff}}=Z_1$ will not work. Instead, the following procedure was found to provide values for Z_{eff} that gave reasonably good projectile scaling. Because the Al data points sampled the highest V region, where the V dependence is nearly constant, the four cross sections measured at 10, 15, 20, and 25 MeV/amu were chosen to establish the average Z_{eff} scaling factors, defined as

$$Z_{\mathrm{eff}} = \{\sigma_{K\alpha}(Z_1)/[\omega_0 \sigma_K(1)]\}^{1/2}, \tag{9}$$

where $\sigma_{K\alpha}(Z_1)$ is the Al $K\alpha$ x-ray production cross section for a projectile with atomic number Z_1 and $\sigma_K(1)$ is the Al ECPSSR K-shell ionization cross section for protons. The fully scaled cross sections are shown in Fig. 8 as a function of V. It is found that dividing the data in Fig. 7 by Z_{eff}^2 has the effect of grouping most of the data points for all three projectiles along a "universal" curve. A fit to the data points (which excluded the Al points for the measurements at 2.5, 4, and 6 MeV/amu) using an extreme value four-parameter

TABLE VI. Average absolute deviations of the $K\alpha$ x-ray production cross sections calculated using Eq. (10) from the experimental cross sections.

Target	$\Delta\sigma_{K\alpha}$ Ar (%)	$\Delta\sigma_{K\alpha}$ Kr (%)	$\Delta\sigma_{K\alpha}$ Xe (%)	Restrictions
Al	12.6	18.9	25.8	$V>1.8$
Ti	10.9	25.1	35.7	none
Cu	32.0	27.4	12.5	none
Zr	36.9	38.4	26.3	$V>0.3$
Ag	33.1	13.6	34.8	$V>0.3$
Sm	15.8	39.4	33.5	$V>0.3$
Ta	29.0	23.0	18.4	$V>0.2$

tailed function [24] is shown by the solid curve in Fig. 8. The equation of this curve is

$$F(V) = a_0 \exp(B), \tag{10}$$

where $B=(1/a_2a_3)\{-V+a_1+a_2-a_2a_3 \exp[-(V+a_2 \ln a_3 - a_1)/a_2]\}$, with $a_0=0.1133$, $a_1=1.069$, $a_2=0.2336$, and $a_3=4.486$. The average absolute deviations of the $K\alpha$ x-ray production cross sections calculated using Eq. (10) from the experimental cross sections are given in Table VI.

A graph of Z_{eff} versus Z_1 is shown in Fig. 9. The error bars on the data points for Ar, Kr, and Xe represent the standard deviations from the average values of Z_{eff} determined using the four Al cross sections. The other data points in Fig. 9 were calculated using Al cross sections from a previous study [7] at 10 MeV/amu that were reevaluated to include the double K-vacancy production contributions. The equation of the fitted solid curve in this figure is

$$Z_{\text{eff}} = 46.29[1 - \exp(-0.0256Z_1)]. \tag{11}$$

V. CONCLUSION

By employing an Si(Li) detector to measure the $K\alpha$ x-ray yields and a high-resolution curved crystal spectrometer to examine the structure of the $K\alpha$ x-ray spectra, cross sections for K-vacancy production in targets ranging from Al to Ta by collisions of 2.5–25 MeV/amu Ar, Kr, and Xe ions have been determined. The K-vacancy production cross sections for Ar projectiles were found to agree reasonably well with the predictions of the ECPSSR theory for all the targets except those for Al, which were as much as an order of magnitude lower than the theoretical values at the lowest speed ratios. The cross sections for K-vacancy production in Al and Ti by Kr and Xe projectiles were considerably lower than the ECPSSR cross sections over the whole range of V, while those for Cu, Zr, and Ag were higher than the ECPSSR predictions at low V and lower at high V. The cross sections for Kr on Sm and Ta were in good agreement with theory, but those for Xe on Sm and Ta, which contain substantial contributions from the molecular orbital mechanism, were much larger than the theoretical cross sections below $V=0.4$.

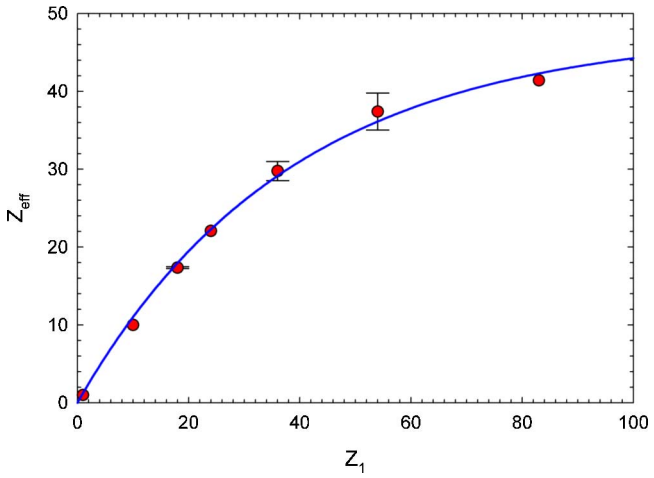

FIG. 9. (Color online) A graph showing the dependence of the projectile effective charge on the projectile atomic number. The solid curve has been fit to the data points.

Examination of the scaling properties of the $K\alpha$ x-ray production cross sections revealed that multiplication by the factor B_K^2/ω_0, for the most part, removes the target dependence. Also, it was found that the projectile dependence is nearly independent of V and can be expressed by a factor representing the square of the projectile *effective* charge (Z_{eff}^2). Thus, multiplying the $K\alpha$ x-ray production cross sections by $B_K^2/(\omega_0 Z_{\text{eff}}^2)$ resulted in the delineation of a semiempirical "universal" function of V. This function may be used to estimate cross sections for other collision systems that have not yet been measured.

ACKNOWLEDGMENT

This work was supported by Grant No. A-0355 from the Robert A. Welch Foundation.

[1] W. E. Meyerhof, R. Anholt, T. K. Saylor, S. M. Lazarus, A. Little, and L. F. Chase, Jr., Phys. Rev. A **14**, 1653 (1976).
[2] W. E. Meyerhof, R. Anholt, and T. K. Saylor, Phys. Rev. A **16**, 169 (1977).
[3] R. Anholt and W. E. Meyerhof, Phys. Rev. A **16**, 190 (1977).
[4] W. E. Meyerhof, R. Anholt, J. Eichler, and A. Salop, Phys. Rev. A **17**, 108 (1978).
[5] R. Anholt, W. E. Meyerhof, Ch. Stoller, E. Morenzoni, S. A. Andriamonje, J. D. Molitoris, O. K. Baker, D. H. H. Hoffmann, H. Bowman, J.-S. Xu, Z.-Z. Xu, K. Frankel, D. Murphy, K. Crowe, and J. O. Rasmussen, Phys. Rev. A **30**, 2234 (1984).
[6] R. L. Watson, J. M. Blackadar, and V. Horvat, Phys. Rev. A **60**, 2959 (1999).
[7] R. L. Watson, V. Horvat, J. M. Blackadar, and K. E. Zaharakis, Phys. Rev. A **62**, 052709 (2000).

[8] G. Basbas, W. Brandt, and R. Laubert, Phys. Rev. A **17**, 1655 (1978).
[9] W. Brandt and G. Lapicki, Phys. Rev. A **23**, 1717 (1981).
[10] G. Lapicki and F. D. McDaniel, Phys. Rev. A **23**, 975 (1981).
[11] Goodfellow Corp., www.goodfellow.com
[12] V. Horvat and R. L. Watson, J. Phys. B **34**, 777 (2001).
[13] V. Horvat, R. L. Watson, and Y. Peng, Phys. Rev. A **74**, 022718 (2006).
[14] J. H. Scofield, Phys. Rev. A **9**, 1041 (1974).
[15] J. H. Hubbell and S. M. Seltzer, at http://physics.nist.gov/PhysRefData/XrayMassCoef/cover.html
[16] V. Horvat, R. L. Watson, and J. M. Blackadar, Nucl. Instrum. Methods Phys. Res. B **170**, 336 (2000).
[17] V. Horvat, R. L. Watson, J. M. Blackadar, A. N. Perumal, and Y. Peng, Phys. Rev. A **71**, 062709 (2005).
[18] B. Sulik, I. Kadar, S. Ricz, D. Varga, J. Vegh, G. Hock, and D. Berenyi, Nucl. Instrum. Methods Phys. Res. B **28**, 509 (1987).
[19] J. H. McGuire and P. Richard, Phys. Rev. A **8**, 1374 (1973).
[20] J. H. Hubbell, P. N. Trehan, N. Singh, B. Chand, D. Mehta, M. L. Garg, R. R. Garg, S. Singh, and S. Puri, J. Phys. Chem. Ref. Data **23**, 339 (1994).
[21] R. L. Watson, V. Horvat, and K. E. Zaharakis, *Proceedings of the 16th International Conference on the Application of Accelerators in Research and Industry*, edited by J. L. Duggan and I. L. Morgan (American Institute of Physics, New York, 2001), p. 93.
[22] V. Horvat, Ž. Šmit, R. L. Watson, A. N. Perumal, and Y. Peng, *Proceedings of the 17th International Conference on the Application of Accelerators in Research and Industry*, edited by J. L. Duggan and I. L. Morgan (American Institute of Physics, New York, 2003), p. 7.
[23] P. Richard, *Atomic Inner-shell Processes*, edited by B. Crasemann (Academic Press, New York, 1975), Vol. I, p. 73.
[24] *PEAKFIT Peak Separation and Analysis Software*, version 4.0 (AISN Software Inc., Jandel Scientific, San Rafael, CA, 1995).